COMMUNICATIONS IN SCIENCE AND TECHNOLOGY
Homepage: cst.kipmi.or.id

Efficient degradation of methyl orange through photo-Fenton processes with MIL-100(Fe) modified Fe_3O_4 (Fe_3O_4@MIL-100(Fe)) catalyst

Melani Puji Puspitasari[a], Jeesica Hermayanti Pratama[a,b], Roshid Adi Nugroho[a], Witri Wahyu Lestari[a,*], Yusnadia Kemala[a], Teguh Endah Saraswati,[a] Hamzah Fansuri[b], Rino Rakhmata Mukti[c], Rujito S. R. Suharbiansah[d]

[a]*Department of Chemistry, Universitas Sebelas Maret, Surakarta 57126, Indonesia.*
[b]*Department of Chemistry, Institut Teknologi Sepuluh Nopember, Surabaya 60111, Indonesia*
[c]*Division of Inorganic and Physical Chemistry, Institut Teknologi Bandung, Bandung 40132, Indonesia*
[d]*Institute of Chemical Technology, Leipzig University, Leipzig 04103, Germany*

Article history:
Received: 5 August 2024 / Received in revised form: 27 October 2024 / Accepted: 31 October 2024

Abstract

The research successfully synthesized a composite MIL-100(Fe) modified Fe_3O_4 (Fe_3O_4@MIL-100(Fe)) catalyst and examined its efficiency in degrading methyl orange (MO) through the photo-Fenton process compared to Fenton. The different percentages of Fe_3O_4 were integrated into MIL-100(Fe) and their effects on material characteristics and degradation capabilities were studied. Ex-situ synthesis involved varying Fe_3O_4 weight ratios (3, 10, and 20% w/w). Characterization techniques confirmed the integration of Fe_3O_4 and MIL-100(Fe) and revealed changes in surface area, pore size, and thermal stability with Fe_3O_4 addition. Meanwhile, removal tests showed promising results with the photo-Fenton process exhibiting maximum efficiency (95.51%) using 10% Fe_3O_4@MIL-100(Fe). This study provides valuable insights into developing efficient photo-Fenton catalysts for environmental remediation, particularly for addressing dye pollution in wastewater by highlighting the potential of Fe_3O_4@MIL-100(Fe) composites in this context.

Keywords: Fe_3O_4; MIL-100(Fe); methyl orange; Fenton; photo-Fenton

1. Introduction

Rapid population growth has exacerbated water pollution, depleting clean water resources. This issue demands a special attention, particularly in view of the significant dye consumption by industries such as textiles, plastics, paper, and leather, which release complex and stable aromatic compounds into wastewater. Methyl orange, which is carcinogenic and mutagenic, is difficult to be removed due to its aromatic structure [1–3]. Advancing technologies to eliminate industrial azo dyes, therefore, is deemed essential [4]. Wastewater treatment technique encompasses adsorption, flocculation, biological processes, and advanced oxidation processes (AOPs) [5,6]. Of these, AOPs, including the Fenton system, are seen highly effective in lowering the levels of toxic organic compounds in wastewater [7,8]. The Fenton process, which relies on the reaction of H_2O_2 with Fe(II) ions to form hydroxyl radicals (•OH), is recognized for its strong oxidizer [9,10]. However, the homogeneous Fenton process using divalent iron salts has a number of drawbacks, including difficulty in catalyst recovery as well as high costs, which can lead to secondary pollution from iron sludge [11]. To address these challenges, alternative technologies such as AOPs are being developed to produce highly active hydroxyl radicals and convert refractory organic matter into less toxic molecules.

The development of catalysts, specifically iron-based heterogeneous Fenton catalysts, aims to address the drawbacks of homogeneous Fenton systems. Heterogeneous Fenton catalysts, such as Fe_3O_4, offer some advantages, including excellent catalytic performance, simple recovery, and applicability across a broad pH range [9]. The efficiency of organic pollutant degradation can be improved by integrating the heterogeneous Fenton process with UV light irradiation, making the photo-Fenton process a focal point in wastewater treatment [13,14]. Combining ultraviolet and visible light with the Fenton process can enhance catalytic performance, boost the efficiency of organic pollutant degradation, and minimize iron sludge generation [10,11]. However, to optimize the heterogeneous photo-Fenton process, addressing the kinetics of the limiting step is crucial for increased activation and H_2O_2 utilization. The photodegradation of compounds under UV

* Corresponding author.
Email: witri@mipa.uns.ac.id
https://doi.org/10.21924/cst.9.2.2024.1493

This open access article is distributed under a Creative Commons Attribution (CC-BY) 4.0 license

light also needs to be concerned as artificial UV lamps require substantial electrical energy, and ultraviolet radiation [15,16]. To overcome these challenges, a more efficient heterogeneous photo-Fenton catalyst is then required.

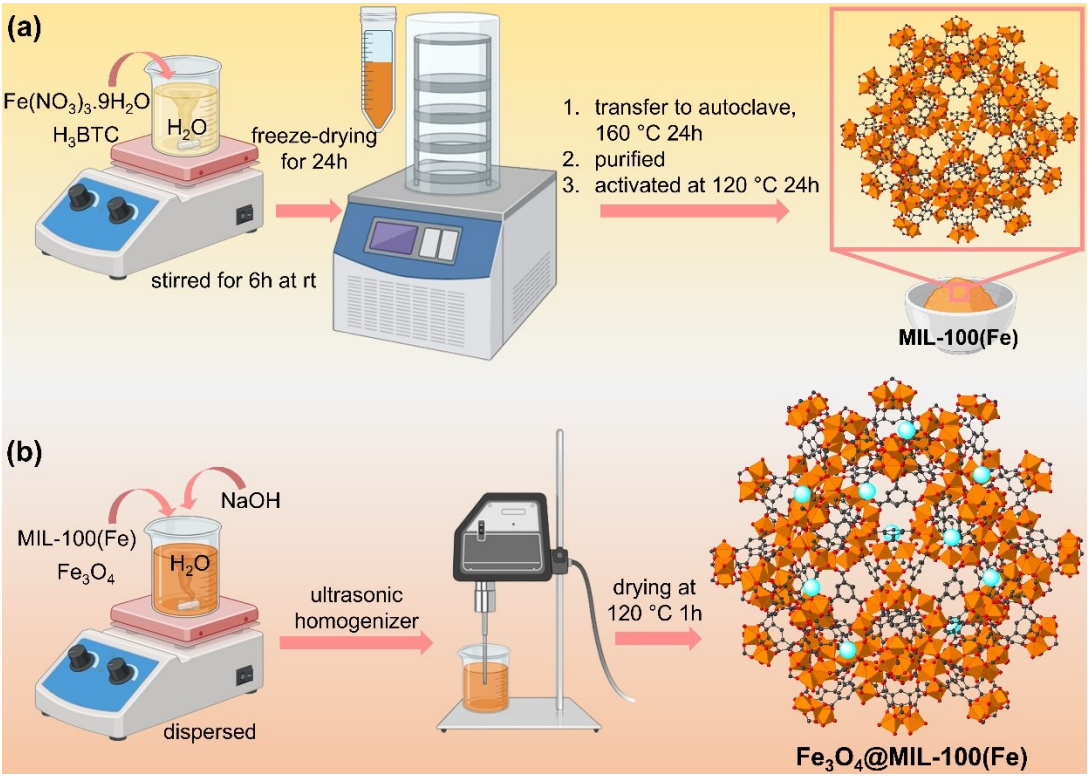

Fig. 1. Schematic illustration for the preparation of (a) MIL-100(Fe) via dry-gel conversion and (b) Fe_3O_4@MIL-100(Fe) via *ex-situ* modification

Various inorganic and organic porous materials have been utilized to modify heterogeneous Fenton catalysts, including organic membranes [16], bentonite [17], zeolite [18], graphene oxide [18], and metal-organic frameworks (MOF) [19]. Modifying the chemical environment in MOF with metal oxides can effectively reduce the rapid recombination of electron-hole pairs. It accelerates the migration of photogenerated electrons and holes, ultimately increasing the rate of photo-Fenton process [20–22]. MOFs have been utilized as catalysts support in Fenton and photo-Fenton reactions, demonstrating their effectiveness in degrading organic dyes. Ding et al., for instance, prepared an innovative Mn-doped Fe-based MOF catalyst with Fenton-like properties, attaining up to 96% efficiency in eliminating organic pollutants from wastewater along with excellent degradation performance, stability, and reusability [23]. In other studies, He et al. developed a hybrid composite, Fe_3O_4@MIL-100(Fe), showing synergistic effects in levofloxacin degradation in the photo-Fenton reaction [24]. Zhang et al. also demonstrated the efficient photo-Fenton performance of Fe_3O_4@MIL-100(Fe), achieving 99.77% degradation of methylene blue within 200 minutes [25]. Additionally, Fe_3O_4@MIL-100(Fe) exhibited an enhanced adsorption capacity for methylene blue, achieving a value of 221 mg/g as reported by Aslam et al.[26]. MIL-100(Fe) exhibits notable water resistance and exceptional stability with a framework composing $[Fe_3O(X)(H_2O)_2]^{6+}$ and H_3BTC, and showcasing a zeotype structure. The modification of Fe_3O_4 with porous inorganic support materials, such as MIL-100(Fe), is anticipated to distribute the Fe_3O_4 catalyst more uniformly. The Lewis acidity present in MOFs, such as MIL-100(Fe), is essential for photo-Fenton reactions and a range of other catalytic processes [27]. Incorporating Fe_3O_4 onto MOFs with acidic surfaces improves the rate constants of the photo-Fenton process for methyl orange degradation by generating •OH radicals. Moreover, the narrow band gap of MIL-100(Fe) (2.04 eV) allows for more efficient visible light absorption, further accelerating the photo-Fenton process [28]. This study aims to examine how the percentage of Fe_3O_4 added to MIL-100(Fe) affects the catalytic performance of photo-Fenton processes and explore their synergistic influence on methyl orange degradation.

2. Materials and Methods

2.1. Materials

All chemicals were used as received without any further purification. They include Iron(III) nitrate nonahydrate ($Fe(NO_3)_3{\cdot}9H_2O$) (Merck, >98%), trimesic acid (H_3BTC) (Sigma-Aldrich, 98%), Fe_3O_4 nanoparticles (Sigma Aldrich, 99% with particle size 50-100 nm), hydrochloric acid (HCl) (Merck, 37%), sodium hydroxide (NaOH) (Merck, 99%), ethanol (C_2H_5OH) (Sigma Aldrich, 96%), N-N'-dimethylformamide (Merck, ≥99%), hydrogen peroxide (H_2O_2) (Merck, 30%), methyl orange (Merck, ≥99%), and deionized water supplied by PT. Kitosa Jaya Cemerlang.

2.2. Synthesis of MIL-100(Fe)

The MIL-100(Fe) synthesis was conducted through the dry-

gel conversion method, as modified from a previous study by Luo et al. [29]. $Fe(NO_3)_3 \cdot 9H_2O$ (10 mmol) and H_3BTC (6.7 mmol) were dissolved in distilled water (18 mL) and vigorously stirred for 6 hours at room temperature. Subsequently, the Fe–BTC mixture was freeze-dried for 24 hours to obtain an orange dry gel sol. Furthermore, the dry gel sol obtained was ground into a powder, transferred to a Teflon autoclave and heated in an UN-30 Memmert oven at a temperature of 160°C for 24 hours. Any residual ligand was purified by rinsing the product three times with distilled water, dimethylformamide (DMF), and ethanol at 65°C for 24 hours. The resultant orange powder was later activated at 120°C for 12 hours to yield the MIL-100(Fe) material. Fig. 1(a) depicts the schematic representation of the preparation procedure for MIL-100(Fe).

2.3. Synthesis of composites Fe_3O_4@MIL-100(Fe)

The Fe_3O_4@MIL-100(Fe) composites were prepared based upon the methodology as outlined by Qian Tang et al. with certain modifications. Fig.1(b) illustrates a schematic diagram for the preparation process of Fe_3O_4@MIL-100(Fe). Variations in the loading of Fe_3O_4 nanoparticles (NPs) were incorporated into MIL-100(Fe) at the concentrations of 3%, 10%, and 20% (w/w) relative to a total composite mass of 1.2 g. Initially, Fe_3O_4 and MIL-100(Fe) were dispersed in 15 mL deionized water. Each mixture was stirred separately for 10 minutes, after which 1 mM NaOH solution was gradually introduced to the Fe_3O_4 solution until the pH approximated 8. The positively charged Fe_3O_4 was then combined with the MIL-100(Fe) solution by means of an ultrasonic homogenizer for a duration of 20 minutes. The resulting samples were subsequently washed three times with deionized water and dried at 120°C for 1 hour.

2.4. Characterization of materials

X-ray diffractograms were recorded using an Expert Pan Analytical system equipped with a Cu Kα detector (λ = 1.5418 Å) and operated at a power of 40 kV, covering a 2θ range of 5–50°. The degree of crystallinity (Xc) of each material is calculated based on Eq. (1).

$$Xc = (A_c / (A_c + A_a)) \; x \; 100 \qquad (1)$$

In this context, A_c denotes the area of the crystalline region, and A_a signifies the area of the amorphous region. The functional groups of the materials were analyzed using Fourier transform infrared (FTIR) spectrometer (Shimadzu IR Prestige-21, Japan with KBr pellets in the range of 400-4000 cm^{-1}). The morphology and particle sizes were observed with the help of a JEOL JIB-4610F Field Emission Scanning Electron Microscope coupled with Energy Dispersive X-ray Spectroscopy (FESEM-EDX). For the detailed analysis of the morphology and distribution of the particles, they were analyzed using Low Resolution-Transmission Electron Microscope (LR-TEM) type HT7700, which operated at 120 kV. Nitrogen sorption isotherms were measured at -196°C utilizing a MicrotracBEL Corp., BELSORP-miniX instrument (Haan/Düsseldorf, Germany). Prior to the measurements, around 100-200 mg of the sample were activated at 150°C under a pressure of 1 P. The total pore volume was determined at the point where P/P^0 = 0.99. The Brunauer-Emmett-Teller (BET) method was employed to determine the specific surface area, while the Barrett-Joyner-Halenda (BJH) method was used to calculate the pore width distribution. The Harkins and Jura model through t-plot analysis was also employed to calculate the micropore volume. The thermal stability of the materials was assessed via Differential Thermal/ Thermogravimetric Analysis (DT/TGA) using a Hitachi STA Linseis PT-1600, conducted from room temperature to 900°C at a heating rate of 10°C per minute under a nitrogen atmosphere. The magnetization values of the materials were measured using a Vibrating Sample Magnetometer (VSM) 250 within an external magnetic field range of 100 Oe to 21 kOe at room temperature.

2.5. Methyl orange (MO) degradation study

The parameters used for the degradation study of MO by Fe_3O_4@MIL-100(Fe) composites included the effects of pH (determination of optimum conditions based on the adsorption method), dye handling method, and contact time. pH of solutions was varied (from pH 2, 4, 6, 8, to 10) to determine the optimum conditions by adding a solution of 0.1 M HCl and 0.1 M NaOH. The dye handling methods applied included the adsorption, Fenton, and photo-Fenton processes. The dye handling study began with an adsorption process for 30 minutes, followed by the advanced handling methods (adsorption, Fenton, and photo-Fenton process) ranging from 0, 30, 60, 90, 120, to 150 minutes at optimum pH conditions.

During the process, 10 mg catalysts were added with 25 mL dye solution and shaken at 120 rpm at a particular time contact, pH, and handling process. The adsorption process was carried out minus the addition of H_2O_2 and without irradiating a Hg lamp. Meanwhile, the Fenton process was carried out by adding H_2O_2 without irradiating a Hg lamp, and the photo-Fenton process was carried out by adding H_2O_2 and by irradiating a Hg lamp 250 watts (with a luminous efficacy of 51 lm/W). Upon the completion of the dye adsorption and degradation tests, the composite samples were removed from the solution through the decantation method. The remaining solution's absorbance was assessed with the aid of a UV-Vis Hitachi UH5000 Spectrophotometer. The absorbance values obtained, later on, were converted to concentration based on the calibration curve (ESI S5). The efficiency of the dye removal process was calculated using Equation (2).

$$\%efficiency = ((C_0 - C_e) / C_0) \; x \; 100 \qquad (2)$$

where C_0 represents the initial concentration and C_e denotes the final concentration of the solutions, measured in parts per million (ppm).

3. Results and Discussion

3.1. Materials characterization

The MIL-100(Fe) synthesis was executed with precision through the dry-gel conversion method, a technique validated through meticulous Powder X-ray Diffraction analysis (Fig. 2(a)). Our synthesized MIL-100(Fe) displayed three distinct characteristic peaks, mirroring closely the highest peak areas documented in the CCDC: 640536 databases. To ensure the

accuracy of our synthesis, we refined the PXRD pattern of MIL-100(Fe) with the use of the Le Bail method by Rietica software [30]. This refinement process involved a dual-phase approach incorporating MIL-100(Fe) and trimesic acid as the ligand precursor. Impressively low residual phase (R_p) and residual weight phase (R_{wp}) with the values of 3.96% and 4.85%, respectively were obtained, attesting to the structural integrity of our synthesized MIL-100(Fe). Furthermore, the goodness of fit (GoF) values, standing at a mere 1.677%, highlighted the remarkable congruence between our synthesized MIL-100(Fe) and the established standard pattern (referring to ESI S1).

The composite Fe_3O_4@MIL-100(Fe) was synthesized via a post-synthesis modification procedure entailing the addition of Fe_3O_4 subsequent to the synthesis of MIL-100(Fe), as illustrated in Fig. 2(a). The introduction of Fe_3O_4 induced the appearance of new peaks while preserving the characteristic peaks of MIL-100(Fe). The analysis of the composite diffractogram revealed distinct peaks attributable to Fe_3O_4, as corroborated by CCDC: 1781925, thus confirming the successful synthesis of the Fe_3O_4@MIL-100(Fe) composite. Notably, all three variants of the Fe_3O_4@MIL-100(Fe) composites exhibited analogous diffraction patterns at 2θ angles of 6.15°, 10.13°, 10.18°, and 35.42°. The intensity of Fe_3O_4 characteristic peaks on the composites diffractogram augmented with the escalating Fe_3O_4 percentages. Furthermore, the degree of crystallinity was determined based upon the ratio of the crystalline phase area to the total area in the diffractogram, as described in Eq. (1). The crystallinity degrees for MIL-100(Fe) and the Fe_3O_4@MIL-100(Fe) composites with 3, 10, and 20% Fe_3O_4 content were 54.75, 40.79, 30.34, and 30.39%, respectively. Specifically, a direct correlation was observed: an increase in the percentage of Fe_3O_4 added led to a reduction in the crystallinity of the resulting composites. The incorporation of Fe_3O_4 into the composite material demonstrated a decreasing effect on its crystallinity in view of the ability of these metal oxides to disrupt the regular lattice of the MIL-100(Fe) framework. This disruption may then result in phase separation or the formation of new phases that do not exhibit the similar crystallinity as the original MOF.

Further characterization using FTIR confirmed the formation of MIL-100(Fe) and its composites with Fe_3O_4 observed from the characteristic absorption peaks from respective materials, as shown in Fig. 2(b). The major bands were attributed to the stretching vibration of O–H, C=O, C-O, and C=C aromatic from the linker and Fe-O bond in MIL-100(Fe). The results align with previous work conducted by previous study [31]. A significant shift in the C=O band from 1723 to 1625 cm^{-1} indicated a deprotonated and coordinated carboxylic moiety with the iron cluster to form MIL-100(Fe). Another shift occurred in wavenumber 2550-3085 cm^{-1} in the ligand to approximately 3393 cm^{-1}, strengthening the hypothesis of deprotonation phenomena and indicating hydrogen bond formation. Fe–O stretching band as the proof of coordination between atoms Fe and O appeared at 483 cm^{-1}, in agreement with a previous study by Mahmoodi et al. [32] that found Fe–O vibration at 481 cm^{-1}. Fe_3O_4@MIL-100(Fe) formation can also be seen from the FTIR analysis. It showed that the Fe_3O_4@MIL-100(Fe) retained the original absorption bands of MIL-100(Fe) and exhibited a weak absorption band of Fe–O at 580 cm^{-1}, reflecting the presence of Fe_3O_4

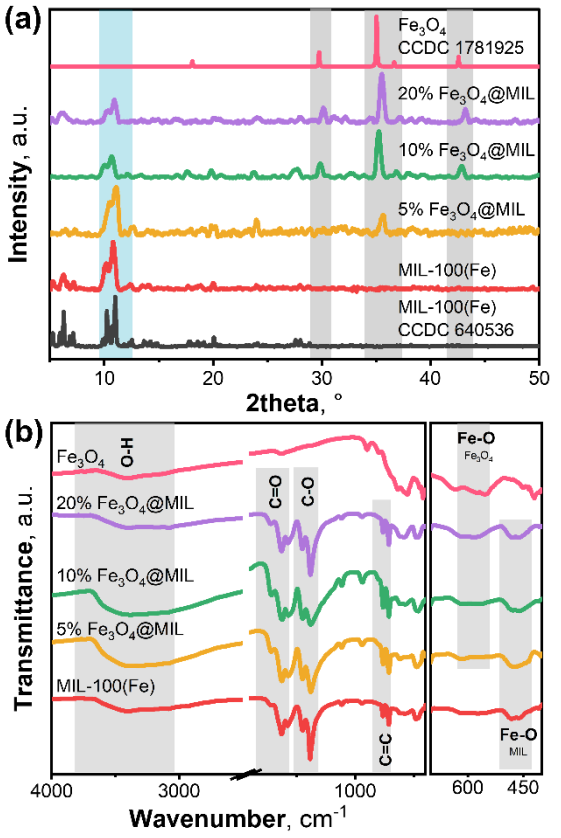

Fig. 2. (a) PXRD pattern and (b) FTIR spectra of MIL-100(Fe) and Fe_3O_4/MIL-100(Fe) composites

The nitrogen sorption isotherms, as presented in Fig. 3(a), for MIL-100(Fe) indicated its classification as a microporous material, as evidenced by the characteristic type I Langmuir isotherm, following the IUPAC classification standards [33]. This microporous behavior persisted even after the formation of Fe_3O_4@MIL-100(Fe) [34]. However, upon the incorporation of Fe_3O_4, the BET surface area of the composites exhibited a gradual decrease from 892.65 m^2/g to 405.93 m^2/g, 772 m^2/g, and 422.53 m^2/g with the addition of 3.0%, 10.0%, and 20.0% Fe_3O_4, respectively. Concurrently, the pore diameter also experienced a reduction from 1.98 nm to 1.49, 1.75, and 1.41 nm as the presence of Fe_3O_4 led to the coverage of pores and surfaces of the host material. Table S3 depicts the detailed values of the BET surface area, pore volume, and pore diameter.

The characterization of the materials was performed with the use of a vibrating-sample magnetometer (VSM) to evaluate their magnetic properties, including saturation magnetization (Ms), remanent magnetization (Mr), and coercivity (Hc). The magnetic properties of Fe_3O_4@MIL-100(Fe) were assessed in conjunction with those of Fe_3O_4 nanoparticles (NPs). As detailed in Table S4 and illustrated in Fig. 3(b), the saturation magnetization of Fe_3O_4@MIL-100(Fe) was found lower than that of Fe_3O_4 nanoparticles. For the 3% Fe_3O_4@MIL-100(Fe), the Ms was recorded at 2.81 emu/g, with a coercivity value of 158.79 Oe and a remanent magnetization value of 0.24 emu/g. For the 10% Fe_3O_4@MIL-100(Fe) composite, the saturation

magnetization (Ms) was recorded at 7.40 emu/g with a coercivity value of 140.08 Oe and a remanent magnetization (Mr) of 0.70 emu/g. In contrast, the 20% Fe_3O_4@MIL-100(Fe) demonstrated a saturation magnetization of 12.87 emu/g along with a coercivity of 143.71 Oe and a remanent magnetization of 1.32 emu/g, indicating an increase in values due to the higher Fe_3O_4 content. The enhancement of magnetic properties in MIL-100(Fe), which is naturally non-magnetic, allows for the straightforward separation of catalysts through the application of an external magnetic field. This not only simplifies catalyst recovery but also has the potential to improve the efficiency of pollutant degradation in advanced oxidation processes.

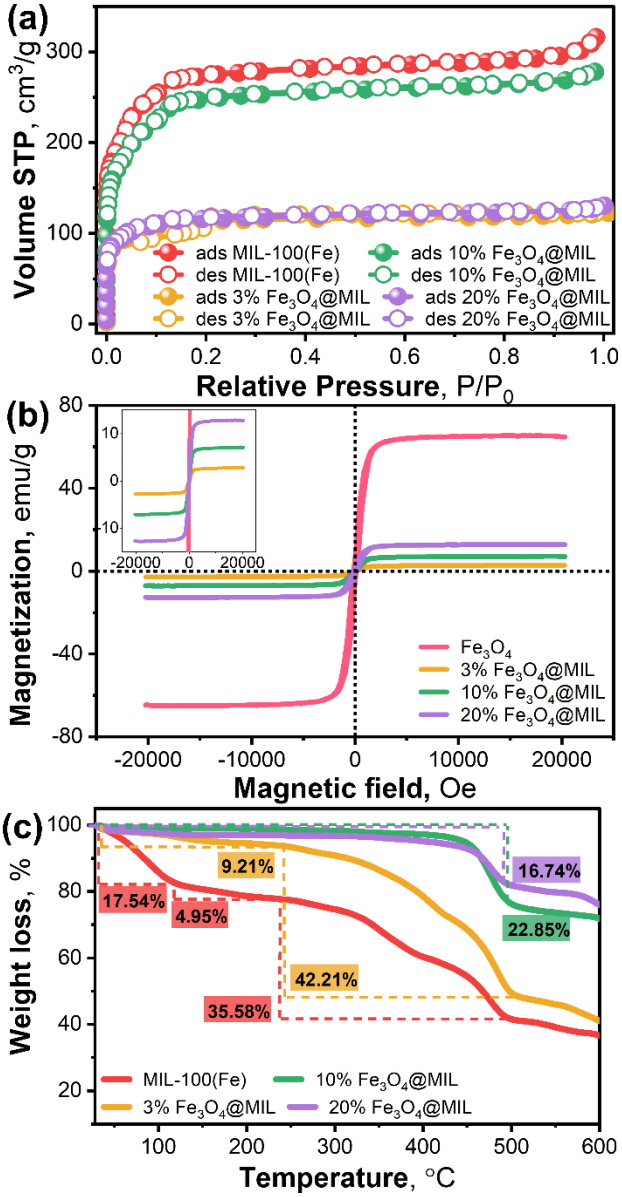

Fig. 3. (a) Nitrogen adsorption-desorption isotherm, (b) magnetization hysteresis curves, and (c) TG thermogram of MIL-100(Fe) and Fe_3O_4@MIL-100(Fe) composites

These findings emphasized the effective synthesis of the Fe_3O_4@MIL-100(Fe) composite and showcased its unique magnetic properties in comparison to Fe_3O_4 nanoparticles (NPs). The impact of Fe_3O_4 addition to the support material on thermal properties was investigated in this study. As depicted in Fig. 3(c), Fe_3O_4@MIL-100(Fe) exhibited superior thermal resistance compared to MIL-100(Fe). The 3% Fe_3O_4@MIL-100(Fe) thermogram revealed two distinct weight loss events. The first event occurred within the temperature in the range of 25-300°C, resulting in a weight loss of 9.21%, indicative of the removal of water from the iron trimer unit secondary building unit. The second one, as observed at temperatures exceeding 300°C, amounted to 49.76%, suggesting the decomposition of the BTC linker. In contrast, composites 10% Fe_3O_4@MIL-100(Fe) and 20% Fe_3O_4@MIL-100(Fe) exhibited a single weight loss event occurring at approximately 500°C, indicating the absence of solvents or water due to coverage by Fe_3O_4. The total weight loss at 600°C was 58.67% for 3% Fe_3O_4@MIL-100(Fe), 22.85% for 10% Fe_3O_4@MIL-100(Fe), 16.74% for 20% Fe_3O_4@MIL-100(Fe), while MIL-100(Fe) experienced a loss of 59.89% [35]. This increase in degradation temperature could be attributed to the presence of Fe_3O_4 covering the surface of MIL-100(Fe), which diminished the combustion energy and impeded the combustion process. Furthermore, the higher residue content observed with increased Fe_3O_4 addition may originate from iron oxide.

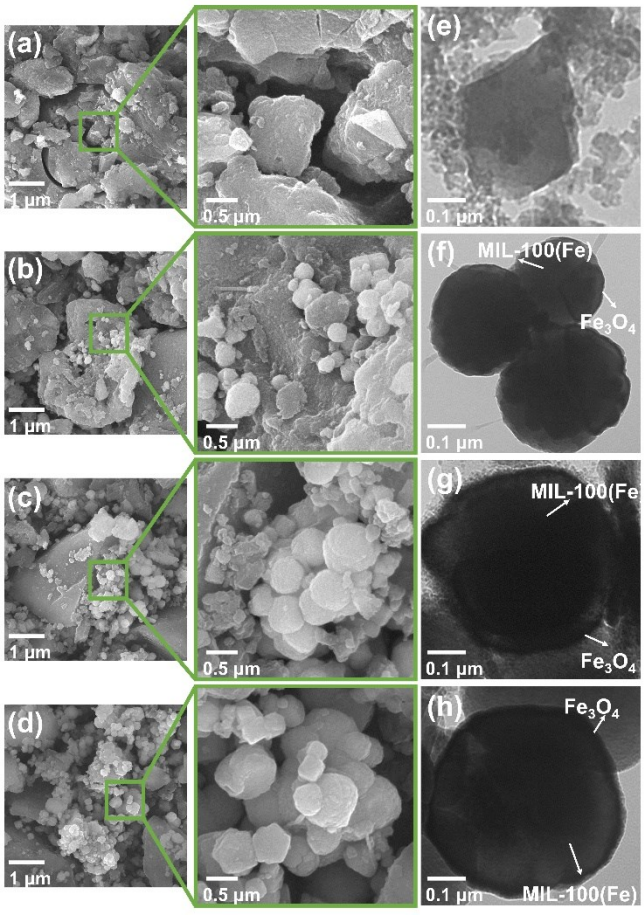

Fig. 4. FESEM and TEM images of (a,e) MIL-100(Fe), (b,f) 3% Fe_3O_4@MIL-100(Fe), (c,g) 10% Fe_3O_4@MIL-100(Fe), and (d,h) 20% Fe_3O_4@MIL-100(Fe)

The material morphology and microstructure were investigated through advanced techniques such as FESEM-EDX and TEM. Remarkably, FESEM-EDX analysis unveiled an intriguing irregular morphology of the synthesized MIL-100(Fe), as depicted in Fig. 4(a), shedding light on the

material's elemental composition. However, this morphology diverged significantly from prior findings, notably those reported by Forghani et al., primarily due to the absence of HF as a modulator during synthesis [36]. Insights from Guo et al. postulated HF's pivotal role as a modulator, intricately influencing nucleation and growth rates by modulating the deprotonation level of H_3BTC, thus intricately shaping the crystallinity phase of MIL-100(Fe) [37]. In our study, the synthesized MIL-100(Fe) showcased non-uniform particle sizes, ranging from 6.52 to 33.90 nm, as revealed by FESEM imaging and particle distribution analysis (ESI S2). Furthermore, the examination of the Fe_3O_4@MIL-100(Fe) composites, as portrayed in Fig. 4(b-d), unveiled the seamless integration of Fe_3O_4 onto the MIL-100(Fe) surface, affirming successful composite synthesis while preserving MIL-100(Fe)'s morphology. Notably, EDX analysis corroborated the increased presence of Fe_3O_4 within the composite, indicative of varying percentages of Fe_3O_4 incorporation (Table S2). Delving deeper into the structural intricacies, TEM analysis (Fig. 4(e-h)) revealed a fascinating core-shell architecture within the composite. Here, Fe_3O_4 particles were observed intricately attached and encapsulated within MIL-100(Fe)'s surface and pore regions, hinting at a complex interplay of surface interactions and composite formation mechanisms. The increased Fe_3O_4 content made the shell structure thicker, and the distinction between the core and shell became more defined. This suggests that adding Fe_3O_4 in optimal amount significantly enhances the performance of the advanced oxidation process.

3.2. Methyl orange (MO) degradation study

3.2.1. Optimization of pH Solution

The pH of a solution stands as a pivotal determinant in the realm of photocatalytic degradation, wielding considerable influence over the kinetics of dye elimination. Acting as a fundamental parameter, solution pH intricately governs both the adsorption and degradation processes, owing to its pronounced impact on the charge dynamics and structural stability of the composite material, alongside the electrochemical characteristics of the dye solution itself. The quest for pH optimization unveils a dynamic interplay between the composite's surface properties and the dye's molecular constitution. A detailed exploration unfolds through meticulous experimentation spanning a pH spectrum encompassing 2, 4, 6, 8, and 10, conducted over a time frame of 30 minutes, with an initial methyl orange (MO) concentration set at 10 ppm. The resulting data, vividly illustrated in Fig. 5(a), charts an intricate relationship between pH modulation and adsorption. Notably, the adsorption of methyl orange dye, facilitated by a 10% Fe_3O_4@MIL-100(Fe) composite, reached its zenith at pH 4, boasting an impressive adsorption efficiency of 56.35%. Thus, pH 4 emerged as a coveted spot, reflecting an optimal balance between composite performance and solution. Moreover, a fascinating trend emerged as the adsorption efficiency of MO exhibited an upward trajectory with escalating solution pH, peaking within the pH range of 2 to 4. However, beyond this threshold, a curious decline in adsorption efficiency ensued, teasing at the intricate interplay of surface interactions and electrochemical forces underpinning the adsorption phenomenon.

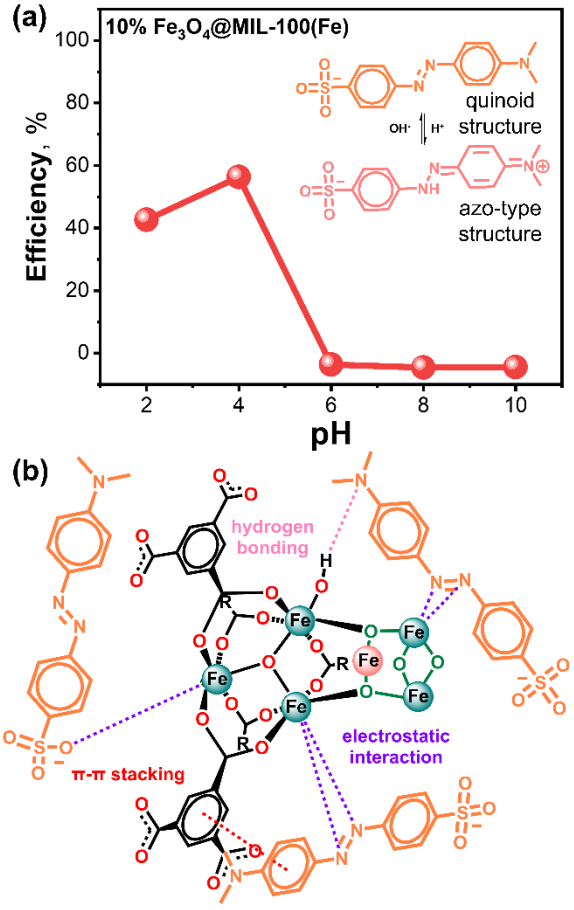

Fig. 5. (a) pH effect on methyl orange adsorption with the structural representation of methyl orange at acidic and basic pH. (b) Schematic illustration of methyl orange adsorption onto Fe_3O_4@MIL-100(Fe)

Fig. 5(b) elucidates the interaction dynamics during the adsorption process. Notably, the surface of Fe_3O_4@MIL-100(Fe) exhibited a positive charge, facilitating its engagement with anionic MO dye through diverse mechanisms, including electrostatic interactions and hydrogen bonding [38]. Lim et al. supposed that the adsorbent demonstrates heightened positivity at lower pH values, thereby augmenting adsorption efficiency [39]. This phenomenon is intriguingly correlated with the dissociation constant (pKa) of MO, approximately 3.20. In solutions where pH exceeds pKa, the MO a negative charge, while below pKa, MO undergoes protonation, signified by a color transition to red, suggesting the diminished electrostatic interactions. The structural variations of methyl orange under acidic and basic conditions are visually depicted in Fig. 5(a). Remarkably, the adsorption efficiency for methyl orange dye showed a significant increase as the pH of the solution rose from 2 to 4, and it decreased at pH levels below 4. At pH < 4, the surface of MIL-100(Fe) had a positive charge, while methyl orange (MO) existed in the quinoid (cationic) form, leading to a repulsive interaction. A similar situation arose at pH > 4, where the surface of MIL-100(Fe) became negatively charged, and MO transitions to the azo (anionic) form, resulting in repulsive interactions. However, at pH 4, the surface of MIL-100(Fe) exhibited only a slight negative charge, and MO

remained in the quinoid form, facilitating an attractive electrostatic interaction between MIL-100(Fe) and MO [41,42]. Furthermore, hydrogen bonding interactions significantly influenced the adsorption capacity of Fe_3O_4@MIL-100(Fe) for methyl orange. Specifically, the -OH functional group within the Fe_3O_4@MIL-100(Fe) formed bonds with oxygen or nitrogen atoms within the methyl orange, thereby impacting the adsorption process. Additionally, π-π stacking interactions between aromatic moieties in Fe_3O_4@MIL-100(Fe) and MO dye further contribute to the intricate adsorption mechanism [42].

3.2.2. MO Degradation Study

Fig. 6 illustrates the efficiency percentages of the adsorption and degradation processes for methyl orange employing Fe_3O_4@MIL-100(Fe) over different time intervals with the maximum efficiency as displayed in Table 1. Remarkably, Fe_3O_4@MIL-100(Fe), after 150 minutes, exhibited peak adsorption efficiency. Of the Fe_3O_4@MIL-100(Fe) composites investigated, the 3% Fe_3O_4@MIL-100(Fe) composite emerged as the frontrunner, boasting an impressive efficiency of 40.86%, surpassing its counterparts such as the 10% Fe_3O_4@MIL-100(Fe) composite and the 20% Fe_3O_4@MIL-100(Fe) composite at 24.41% and 15.59%, respectively. This superiority was attributed to the enhanced accessibility of pores within the 3% Fe_3O_4@MIL-100(Fe) composite, offering a greater surface area for interaction with methyl orange molecules compared to other compositions. The presence of Fe_3O_4 exerted a significant influence on the support material, influencing both adsorption and degradation processes, particularly in Fenton and photo-Fenton reactions. Interestingly, a higher concentration of Fe_3O_4 on the support material may initially hinder optimal adsorption by potentially occluding surface sites or pores. However, this phenomenon paradoxically enhances degradation processes, suggesting a delicate balance between adsorption and degradation kinetics in the Fe_3O_4@MIL-100(Fe) composite system.

Table 1. Maximum efficiency (Eff.) of the composite in various processes.

Composite	Adsorption		Fenton		Photo-Fenton	
	Eff. (%)	t (min)	Eff. (%)	t (min)	Eff. (%)	t (min)
H_2O_2	-	-	2.04	150	23.38	150
Fe_3O_4	-	-	0	150	32.41	150
3% Fe_3O_4@MIL-100(Fe)	40.86	180	56.42	150	92.74	150
10% Fe_3O_4@MIL-100(Fe)	24.41	180	24.76	150	95.51	150
20% Fe_3O_4@MIL-100(Fe)	15.59	180	43.74	150	91.92	150

The efficacy of the Fenton process in degrading methyl orange dye surpassed that of the adsorption method, showcasing remarkable efficiency. Specifically, 3% Fe_3O_4@MIL-100(Fe) demonstrated the highest degradation capacity, reaching approximately 56.42%. This was followed by 20% Fe_3O_4@MIL-100(Fe) at approximately 43.74%, and 10% Fe_3O_4@MIL-100(Fe) at roughly 27.76%. The proposed degradation mechanism primarily hinges on the highly reactive hydroxyl radical (•OH). In the presence of hydrogen peroxide (H_2O_2), ferric ions are reduced to ferrous ions, initiating a cascade of reactions yielding electrons and OH radicals. These •OH radicals are pivotal in dismantling the methyl orange molecules, driving the degradation process forward. The complex series of chemical transformations in the Fenton process is captivating. As depicted in Eq. (3) to (5), the generated electrons catalyze the breakdown of hydrogen peroxide into OH radicals, fueling the degradation reaction. Fig. 7(a) offers a visual narrative of this intricate proposed mechanism, revealing the nuanced interplay of molecular interactions fundamental to the Fenton process.

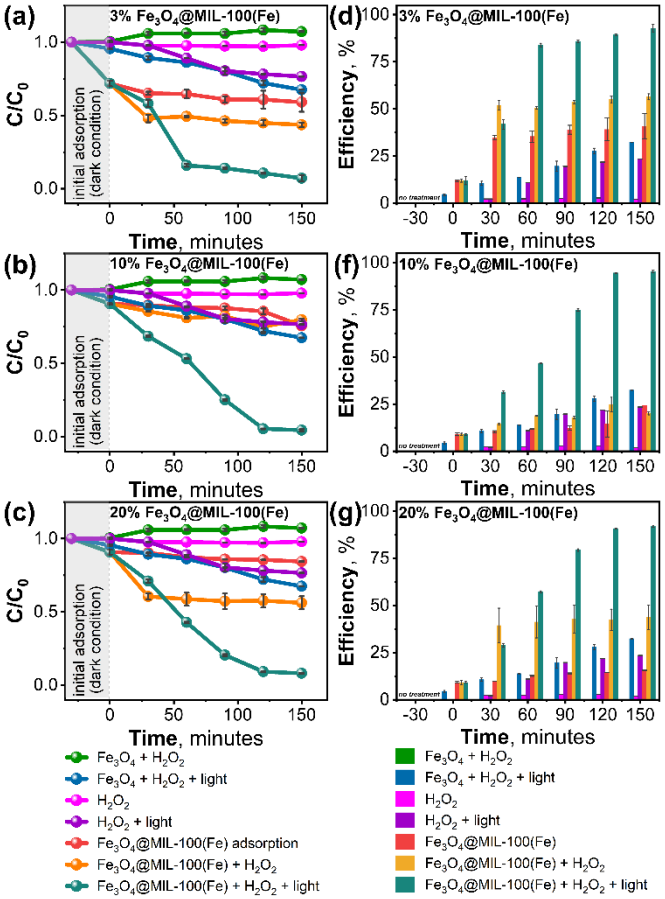

Fig. 6. Efficiency percentage of methyl orange removal by (a,d) 3% Fe_3O_4@MIL-100(Fe), (b,e) 10% Fe_3O_4@MIL-100(Fe), and (c,d) 20% Fe_3O_4@MIL-100(Fe) in various processes

$$Fe(III)_{(aq)} + H_2O_{2(aq)} \rightarrow Fe(II)_{(aq)} + HOO\bullet + H^+_{(aq)} \quad (3)$$

$$Fe(II)_{(aq)} + H_2O_{2(aq)} \rightarrow \bullet OH + Fe(III)_{(aq)} + OH^-_{(aq)} + e^- \quad (4)$$

$$H_2O_{2(aq)} + e^- \rightarrow \bullet OH + OH^-_{(aq)} \quad (5)$$

The photo-Fenton process outshines both Fenton and adsorption methods in the degradation of methyl orange, boasting unparalleled efficiency. The 10% Fe_3O_4@MIL-100(Fe) composite exhibited the highest removal capacity, achieving an outstanding efficiency of 95.51%. Following it closely, the 3% Fe_3O_4@MIL-100(Fe) composite demonstrated an efficiency of 92.74%, while the 20% Fe_3O_4@MIL-100(Fe) composite achieved an efficiency of 91.92%. This heightened

efficacy of the photo-Fenton process can be attributed to its robust OH radical production, facilitating swift degradation compared to alternative methods. The process unfolded rapidly, outpacing its counterparts. As illustrated in Fig. 7(b), the proposed mechanism of methyl orange removal catalyzed by Fe_3O_4@MIL-100(Fe) over the photo-Fenton process captivated. The rupture of the −N=N− bond in methyl orange initiated the formation of intermediate products, such as benzene. These intermediates engaged with OH radicals, inducing further degradation by cleaving the aromatic ring, yielding CO_2 and H_2O [43]. This intricate cascade of reactions underscores the efficacy and potential of the photo-Fenton method in wastewater handling.

$$Fe_3O_4@MIL\text{-}100(Fe)_{(s)} + hv \rightarrow h^+ + e^- \quad (6)$$

$$H_2O_{2(aq)} + e^- (Fe_3O_4@MIL\text{-}100(Fe)) \rightarrow \bullet OH + OH^-_{(aq)} \quad (7)$$

$$O_{2(g)} + e^- \rightarrow O_2^- \quad (8)$$

$$h^+(Fe_3O_4@MIL\text{-}100(Fe)) + H_2O_{(l)} \rightarrow \bullet OH + H^+_{(aq)} \quad (9)$$

$$Fe(III)_{(aq)} + H_2O_{2(aq)} \rightarrow Fe(II)_{(aq)} + HOO\bullet + H^+_{(aq)} \quad (10)$$

$$Fe(II)_{(aq)} + H_2O_{2(aq)} \rightarrow Fe(III)_{(aq)} + \bullet OH + H^+_{(aq)} \quad (11)$$

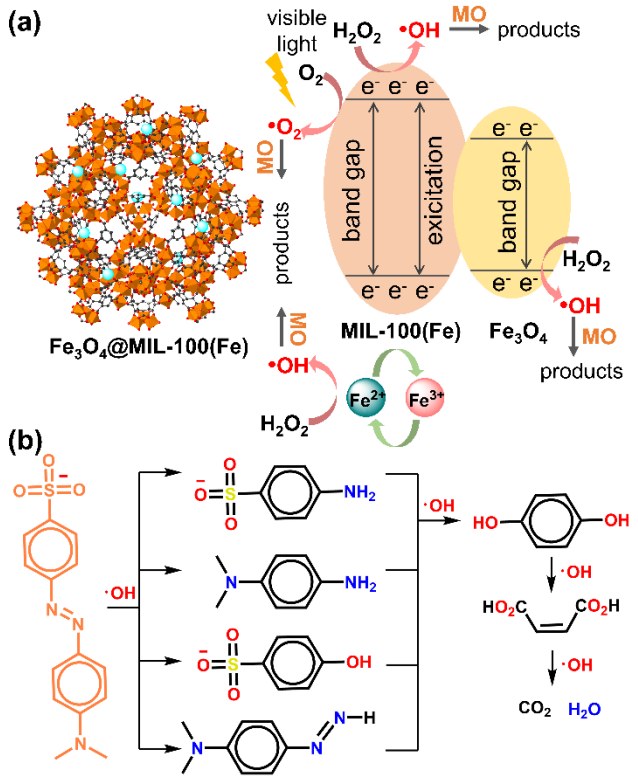

Fig. 7. (a) Scheme of electron excitation in Fenton and photo-Fenton processes, supplemented by (b) scheme depicting methyl orange degradation by the hydroxyl radical

As depicted in Fig. 7(a), the Fe-O bonds within the catalytic system of Fe_3O_4@MIL-100(Fe) were activated by visible light, forming electron (e^-)−hole (h^+) pairs on its surface, as elucidated in Eq. (6). Subsequently, these induced electron (e^-)−hole (h^+) pairs were transferred to both H_2O_2 and Fe_3O_4; the electrons engage with H_2O_2 and O_2, yielding OH radicals and O_2^- radicals, as depicted in Eq. (7) and (8). The hole (h^+) species reacted with H_2O_2 to generate additional OH radicals, as outlined in Eq. (9), while directly oxidizing the methyl orange molecule. Furthermore, the oxidation potential of Fe_3O_4@MIL-100(Fe) enhanced the degradation of MO, as demonstrated in Eq. (10) and (11). These newly formed active species, including •OH radicals, O_2^- radicals, and h^+ holes, collectively drive the degradation of MO into smaller intermediate or final products, such as CO_2 and H_2O [43]. He et al. investigated the formation of the three active species through the photo-Fenton mechanism in Fe_3O_4@MIL-100(Fe) with the results showing that •OH and h^+ played a crucial role in degrading organic pollutants, while $\bullet O^{2-}$ did not significantly contribute to this system [24].

Table 2. Comparison of methyl orange removal efficiency (Eff.) by Fe_3O_4@MIL-100(Fe) and other related materials

Materials	Method	Eff. (%)	t (min)	Ref.
10% Fe_3O_4@MIL-100(Fe)	Photo-Fenton	95.51	150	This study
3% Fe_3O_4@MIL-100(Fe)	Photo-Fenton	92.74	150	This study
MIL-100(Fe)	Adsorption	55	40	[44]
Zeolite NaX	Adsorption	40	35	[45]
Fe_2O_3/active carbon felt	Bio-Electro Fenton	86.7	240	[46]
Si/Al@Fe/MWCNT	Fenton-like oxidation	87	6	[47]
α-Fe_2O_3	Photo-Fenton	76.5	120	[48]

Based on the application studies by adsorption, Fenton, and photo-Fenton process showed that 3% Fe_3O_4 (w/w) in the support material became a compelling composition in the methyl orange removal process since the presence of Fe_3O_4 covered particular pores and could activate the active sites of the material. Both porosity and Lewis acidity of MIL-100(Fe) still could work maximally in the presence of the catalyst. Thus, synergistic effects between adsorption, Fenton, or photo Fenton could proceed physically or chemically. Table 2 shows the reported materials used as catalysts in methyl orange removal. The efficiency percentage of methyl orange removal using Fe_3O_4@MIL-100(Fe) showed the higher results compared to other materials, such as MIL-100(Fe) and Na-X zeolite by adsorption method [45,46], and other degradation methods using Fe_3O_4/active carbon felt [46], Si/Al@Fe/MWCNT [47], and α-Fe_2O_3 [48]. The combination of Fe_3O_4 with MIL-100(Fe) has proven to be an effective catalyst for the photo-Fenton process. The high Fe(II)/Fe(III) content and magnetic properties of Fe_3O_4 play a crucial role in the photo-Fenton reaction. Moreover, MIL-100(Fe) enhances the surface area, making it highly effective as an adsorbent. Additionally, the Fe(III) metal centers in MIL-100(Fe), acting as Lewis acids, can activate substrates, stabilize transition states, and accelerate the production of •OH from H_2O_2 under UV-Vis irradiation [50,51].

4. Conclusion

Composite MIL-100(Fe) modified Fe_3O_4 was successfully prepared and revealed a combination of Fe_3O_4 and MIL-

100(Fe) characteristics as observed in both XRD patterns and FT-IR spectra. The addition of Fe_3O_4 resulted in the decreasing crystallinity of the composite materials. FESEM-EDX and TEM imaging, meanwhile, showed that Fe_3O_4 coated on the external surface of support material confirmed by increasing the Fe and O contained in Fe_3O_4@MIL-100(Fe). The addition of Fe_3O_4 caused the surface area and the pore volume of support material to decrease, while the thermal stability of the composite increased. The presence of Fe_3O_4 in support material affected the removal capacity for methyl oranges. The 3% Fe_3O_4@MIL-100(Fe) showed the best result on the Fenton process with the efficiency of about 56.43%, while the 10% Fe_3O_4@MIL-100(Fe) showed the best result on the photo-Fenton process with the removal efficiency of about 95.51%. The high efficacy of Photo-Fenton for degrading MO suggests promising applications for this material as a filler in mixed matrix membranes. Our research team is currently exploring the role of Fe_3O_4@MOF fillers in these membranes.

Acknowledgements

We wish to express our gratitude to Center for Research and Community Engagement (LPPM) Universitas Sebelas Maret (UNS) for providing research funding through the Program Penelitian Kolaborasi Indonesia (PPKI) 2021, project number 102.1/UN27.22/HK.07.00/2021, in collaboration with the Chemistry Department of Institut Teknologi Sepuluh November (ITS Surabaya) and Institut Teknologi Bandung (ITB), as well as the Applied University Research Grant 2023, project number 228/UN27.22/PT.01.03/2023.

References

1. T. Huang, L. Liu, J. Tao, L. Zhou, and S. Zhang, *Microbial fuel cells coupling with the three-dimensional electro-Fenton technique enhances the degradation of methyl orange in the wastewater*, Environ. Sci. Pollut. Res. 25 (2018) 17989–18000.
2. R. D. Suryavanshi, S. V. Mohite, A. A. Bagade, and K. Y. Rajpure, *Photoelectrocatalytic activity of spray deposited Fe_2O_3/ZnO photoelectrode for degradation of salicylic acid and methyl orange dye under solar radiation*, Mater. Sci. Eng. B 248 (2019) 114386.
3. O. A. Saputra, M. Nauqinida, Kurnia, S. Pujiasih, T. Kusumaningsih, and E. Pramono, *Improvement of anionic and cationic dyes removal in aqueous solution by Indonesian agro-waste oil palm empty fruit bunches through silylation approach*, Groundw. Sustain. Dev. 13 (2021) 100570.
4. W. Qu, D. He, H. Huang, Y. Guo, Y. Tang, and R.-J. Song, *Characterization of amino-crosslinked hypromellose and its adsorption characteristics for methyl orange from water*, J. Mater. Sci. 55 (2020) 7268–7282.
5. S. Aslam, F. Subhan, Z. Liu, Z. Yan, A. Ahmad, A. Nazir, et al., *Magnetic Fe_3O_4@MIL-100(Fe) core-shells decorated with gold nanoparticles for enhanced catalytic reduction of 4-nitrophenol and degradation of azo dye*, Colloids Surfaces A Physicochem. Eng. Asp. 660 (2023) 130904.
6. M. Priyadarshini, I. Das, M. M. Ghangrekar, and L. Blaney, *Advanced oxidation processes: Performance, advantages, and scale-up of emerging technologies*, J. Environ. Manage. 316 (2022) 115295.
7. F. E. Titchou, H. Zazou, H. Afanga, J. El Gaayda, R. Ait Akbour, P. V. Nidheesh, et al., *Removal of organic pollutants from wastewater by advanced oxidation processes and its combination with membrane processes*, Chem. Eng. Process. - Process Intensif. 169 (2021) 108631.
8. Y. Deng, and R. Zhao, *Advanced Oxidation Processes (AOPs) in Wastewater Treatment*, Curr. Pollut. Reports 1 (2015) 167–176.
9. Y. Zhu, R. Zhu, Y. Xi, J. Zhu, G. Zhu, and H. He, *Strategies for enhancing the heterogeneous Fenton catalytic reactivity: A review*, Appl. Catal. B Environ. 255 (2019) 117739.
10. M. Zhang, H. Dong, L. Zhao, D. Wang, and D. Meng, *A review on Fenton process for organic wastewater treatment based on optimization perspective*, Sci. Total Environ. 670 (2019) 110–121.
11. X. Wang, X. Zhang, Y. Zhang, Y. Wang, S.-P. Sun, W. D. Wu, et al., *Nanostructured semiconductor supported iron catalysts for heterogeneous photo-Fenton oxidation: a review*, J. Mater. Chem. A 8 (2020) 15513–15546.
12. R. M. Iqbal, S. D. Nurherdiana, M. S. Sahasrikirana, L. Harmelia, W. P. Utomo, E. P. Setyaningsih, et al., *The Compatibility of NiO, CeO_2 and NiO-CeO_2 as a Coating on $La_{0.6}Sr_{0.4}Co_{0.2}Fe_{0.8}O_{3-\delta}$, $La_{0.7}Sr_{0.3}Co_{0.2}Fe_{0.8}O_{3-\delta}$ and $La_{0.7}Sr_{0.3}Mn_{0.3}O_{3-\delta}$ Ceramic Membranes and Their Mechanical Properties*, IOP Conf. Ser. Mater. Sci. Eng. 367 (2018) 012032.
13. X. Guo, K. Wang, and Y. Xu, *Tartaric acid enhanced $CuFe_2O_4$-catalyzed heterogeneous photo-Fenton-like degradation of methylene blue*, Mater. Sci. Eng. B 245 (2019) 75–84.
14. F. Machado, A. C. S. C. Teixeira, and L. A. M. Ruotolo, *Critical review of Fenton and photo-Fenton wastewater treatment processes over the last two decades*, Int. J. Environ. Sci. Technol. 20 (2023) 13995–14032.
15. X. Wang, W. Liu, J. Qin, and L. Lei, *Improvement of H_2O_2 Utilization by the Persistent Heterogeneous Fenton Reaction with the Fe_3O_4 -Zeolite-Cyclodextrin Composite*, Ind. Eng. Chem. Res. 59 (2020) 2192–2202.
16. F. F. Dias, A. A. S. Oliveira, A. P. Arcanjo, F. C. C. Moura, and J. G. A. Pacheco, *Residue-based iron catalyst for the degradation of textile dye via heterogeneous photo-Fenton*, Appl. Catal. B Environ. 186 (2016) 136–142.
17. A. Jonidi Jafari, B. Kakavandi, N. Jaafarzadeh, R. Rezaei Kalantary, M. Ahmadi, and A. Akbar Babaei, *Fenton-like catalytic oxidation of tetracycline by AC@Fe_3O_4 as a heterogeneous persulfate activator: Adsorption and degradation studies*, J. Ind. Eng. Chem. 45 (2017) 323–333.
18. F. Riyanti, H. Hasanudin, A. Rachmat, W. Purwaningrum, and P. L. Hariani, *Photocatalytic degradation of methylene blue and Congo red dyes from aqueous solutions by bentonite-Fe_3O_4 magnetic*, Commun. Sci. Technol. 8 (2023) 1–9.
19. N. A. Zubir, C. Yacou, J. Motuzas, X. Zhang, X. S. Zhao, and J. C. Diniz da Costa, *The sacrificial role of graphene oxide in stabilising a Fenton-like catalyst GO–Fe_3O_4*, Chem. Commun. 51 (2015) 9291–9293.
20. W. W. Lestari, M. C. Ningrum, R. A. Nugroho, T. E. Saraswati, and S. Wahyuningsih, *Efficient Photo-Fenton Degradation of Eosin Yellow with Solvent-Free Synthesized Fe_3O_4/MIL-100(Cr)*, J. Inorg. Organomet. Polym. Mater. (2024) doi: 10.1007/s10904-024-03360-5.
21. Z. Xue, K. Liu, Q. Liu, Y. Li, M. Li, C.-Y. Su, et al., *Missing-linker metal-organic frameworks for oxygen evolution reaction*, Nat. Commun. 10 (2019) 5048.
22. C. Zhao, J. Wang, X. Chen, Z. Wang, H. Ji, L. Chen, et al., *Bifunctional $Bi_{12}O_{17}Cl_2$/MIL-100(Fe) composites toward photocatalytic Cr(VI) sequestration and activation of persulfate for bisphenol A degradation*, Sci. Total Environ. 752 (2021) 141901.
23. M. Ahmad, S. Chen, F. Ye, X. Quan, S. Afzal, H. Yu, et al., *Efficient photo-Fenton activity in mesoporous MIL-100(Fe) decorated with ZnO nanosphere for pollutants degradation*, Appl. Catal. B Environ. 245 (2019) 428–438.

24. J. Ding, Y.-G. Sun, and Y.-L. Ma, *Highly Stable Mn-Doped Metal–Organic Framework Fenton-Like Catalyst for the Removal of Wastewater Organic Pollutants at All Light Levels*, ACS Omega 6 (2021) 2949–2955.
25. W. He, Z. Li, S. Lv, M. Niu, W. Zhou, J. Li, et al., *Facile synthesis of Fe_3O_4@MIL-100(Fe) towards enhancing photo-Fenton like degradation of levofloxacin via a synergistic effect between Fe_3O_4 and MIL-100(Fe)*, Chem. Eng. J. 409 (2021) 128274.
26. C.-F. Zhang, L.-G. Qiu, F. Ke, Y.-J. Zhu, Y.-P. Yuan, G.-S. Xu, et al., *A novel magnetic recyclable photocatalyst based on a core–shell metal–organic framework Fe_3O_4@MIL-100(Fe) for the decolorization of methylene blue dye*, J. Mater. Chem. A 1 (2013) 14329.
27. S. Aslam, J. Zeng, F. Subhan, M. Li, F. Lyu, Y. Li, et al., *In situ one-step synthesis of Fe_3O_4@MIL-100(Fe) core-shells for adsorption of methylene blue from water*, J. Colloid Interface Sci. 505 (2017) 186–195.
28. W. Wang, D. Chen, F. Li, X. Xiao, and Q. Xu, *Metal-organic-framework-based materials as platforms for energy applications*, Chem 10 (2024) 86–133.
29. Q. Han, Y. Dong, C. Xu, Q. Hu, C. Dong, X. Liang, et al., *Immobilization of Metal–Organic Framework MIL-100(Fe) on the Surface of $BiVO_4$: A New Platform for Enhanced Visible-Light-Driven Water Oxidation*, ACS Appl. Mater. Interfaces 12 (2020) 10410–10419.
30. X. Qian Tang, Y. Dan Zhang, Z. Wei Jiang, D. Mei Wang, C. Zhi Huang, and Y. Fang Li, *Fe_3O_4 and metal–organic framework MIL-101(Fe) composites catalyze luminol chemiluminescence for sensitively sensing hydrogen peroxide and glucose*, Talanta 179 (2018) 43–50.
31. B. A. Hunter, "Rietica - a visual Rietveld program" in *2nd AINSE Symposium on Neutron Scattering Powder Diffraction and Australian Neutron Beam Users Group Meeting Symposium Handbook*, p. 24.
32. A. Amalia, W. W. Lestari, J. H. Pratama, F. R. Wibowo, L. Larasati, and T. E. Saraswati, *Modification of dry-gel synthesized MIL-100(Fe) with carboxymethyl cellulose for curcumin slow-release*, J. Polym. Res. 29 (2022) 487.
33. N. M. Mahmoodi, J. Abdi, M. Oveisi, M. Alinia Asli, and M. Vossoughi, *Metal-organic framework (MIL-100(Fe)): Synthesis, detailed photocatalytic dye degradation ability in colored textile wastewater and recycling*, Mater. Res. Bull. 100 (2018) 357–366.
34. M. Thommes, K. Kaneko, A. V. Neimark, J. P. Olivier, F. Rodriguez-Reinoso, J. Rouquerol, et al., *Physisorption of gases, with special reference to the evaluation of surface area and pore size distribution (IUPAC Technical Report)*, Pure Appl. Chem. 87 (2015) 1051–1069.
35. J. Wang, and X. Guo, *Adsorption isotherm models: Classification, physical meaning, application and solving method*, Chemosphere 258 (2020) 127279.
36. M. Sturini, C. Puscalau, G. Guerra, F. Maraschi, G. Bruni, F. Monteforte, et al., *Combined Layer-by-Layer/Hydrothermal Synthesis of Fe_3O_4@MIL-100(Fe) for Ofloxacin Adsorption from Environmental Waters*, Nanomaterials 11 (2021) 3275.
37. M. Forghani, A. Azizi, M. J. Livani, and L. A. Kafshgari, *Adsorption of lead(II) and chromium(VI) from aqueous environment onto metal-organic framework MIL-100(Fe): Synthesis, kinetics, equilibrium and thermodynamics*, J. Solid State Chem. 291 (2020) 121636.
38. X.-Z. Guo, S.-S. Han, J.-M. Yang, X.-M. Wang, S.-S. Chen, and S. Quan, *Effect of Synergistic Interplay between Surface Charge, Crystalline Defects, and Pore Volume of MIL-100(Fe) on Adsorption of Aqueous Organic Dyes*, Ind. Eng. Chem. Res. 59 (2020) 2113–2122.
39. M. A. Mannaa, K. F. Qasim, F. T. Alshorifi, S. M. El-Bahy, and R. S. Salama, *Role of NiO Nanoparticles in Enhancing Structure Properties of TiO_2 and Its Applications in Photodegradation and Hydrogen Evolution*, ACS Omega 6 (2021) 30386–30400.
40. S. Lim, J. L. Shi, U. von Gunten, and D. L. McCurry, *Ozonation of organic compounds in water and wastewater: A critical review*, Water Res. 213 (2022) 118053.
41. F.-C. Tsai, Y. Xia, N. Ma, J.-J. Shi, T. Jiang, T.-C. Chiang, et al., *Adsorptive removal of acid orange 7 from aqueous solution with metal–organic framework material, iron (III) trimesate*, Desalin. Water Treat. 57 (2016) 3218–3226.
42. X. Jia, X. Chen, Y. Liu, B. Zhang, H. Zhang, and Q. Zhang, *Hydrophilic Fe_3O_4 nanoparticles prepared by ferrocene as high-efficiency heterogeneous Fenton catalyst for the degradation of methyl orange*, Appl. Organomet. Chem. 33 (2019).
43. H. Molavi, A. Hakimian, A. Shojaei, and M. Raeiszadeh, *Selective dye adsorption by highly water stable metal-organic framework: Long term stability analysis in aqueous media*, Appl. Surf. Sci. 445 (2018) 424–436.
44. Y. Fu, S. Shan, F. Chen, and J. Hu, *Constructing an efficient p–n heterojunction photocatalyst $CaFe_2O_4/Fe_2O_3$ nanocomposite for degradation of methyl orange*, J. Mater. Sci. Mater. Electron. 31 (2020) 17967–17979.
45. F. Mahmoudi, M. M. Amini, and M. Sillanpää, *Hydrothermal synthesis of novel MIL-100(Fe)@SBA-15 composite material with high adsorption efficiency towards dye pollutants for wastewater remediation*, J. Taiwan Inst. Chem. Eng. 116 (2020) 303–313.
46. D. Mirzaei, A. Zabardasti, Y. Mansourpanah, M. Sadeghi, and S. Farhadi, *Efficacy of Novel NaX/MgO–TiO_2 Zeolite Nanocomposite for the Adsorption of Methyl Orange (MO) Dye: Isotherm, Kinetic and Thermodynamic Studies*, J. Inorg. Organomet. Polym. Mater. 30 (2020) 2067–2080.
47. T. Ling, B. Huang, M. Zhao, Q. Yan, and W. Shen, *Repeated oxidative degradation of methyl orange through bio-electro-Fenton in bioelectrochemical system (BES)*, Bioresour. Technol. 203 (2016) 89–95.
48. M. Arshadi, M. K. Abdolmaleki, F. Mousavinia, A. Khalafi-Nezhad, H. Firouzabadi, and A. Gil, *Degradation of methyl orange by heterogeneous Fenton-like oxidation on a nano-organometallic compound in the presence of multi-walled carbon nanotubes*, Chem. Eng. Res. Des. 112 (2016) 113–121.
49. A. M. G. Domacena, C. L. E. Aquino, and M. D. L. Balela, *Photo-Fenton Degradation of Methyl Orange Using Hematite (α-Fe_2O_3) of Various Morphologies*, Mater. Today Proc. 22 (2020) 248–254.
50. L. Wang, W. Qiao, H. Liu, S. Li, J. Wu, and H. Hou, *Synergistic Effects of Lewis Acid–Base Pair Sites─Hf-MOFs with Functional Groups as Distinguished Catalysts for the Cycloaddition of Epoxides with CO_2*, Inorg. Chem. 62 (2023) 3817–3826.
51. A. C. Affam, M. Chaudhuri, and S. R. M. Kutty, *Comparison of Five Advanced Oxidation Processes for Degradation of Pesticide in Aqueous Solution*, Bull. Chem. React. Eng. Catal. 13 (2018) 179–186.